

REPORT DOCUMENTATION PAGE				Form Approved OMB NO. 0704-0188	
<p>The public reporting burden for this collection of information is estimated to average 1 hour per response, including the time for reviewing instructions, searching existing data sources, gathering and maintaining the data needed, and completing and reviewing the collection of information. Send comments regarding this burden estimate or any other aspect of this collection of information, including suggestions for reducing this burden, to Washington Headquarters Services, Directorate for Information Operations and Reports, 1215 Jefferson Davis Highway, Suite 1204, Arlington VA, 22202-4302. Respondents should be aware that notwithstanding any other provision of law, no person shall be subject to any penalty for failing to comply with a collection of information if it does not display a currently valid OMB control number.</p> <p>PLEASE DO NOT RETURN YOUR FORM TO THE ABOVE ADDRESS.</p>					
1. REPORT DATE (DD-MM-YYYY)		2. REPORT TYPE		3. DATES COVERED (From - To)	
		New Reprint		-	
4. TITLE AND SUBTITLE Fully coupled thermomechanical finite element analysis of material evolution during friction-stir welding of AA5083				5a. CONTRACT NUMBER	
				W911NF-11-1-0207	
				5b. GRANT NUMBER	
6. AUTHORS M Grujicic, T He, G Arakere, H V Yalavarthy, C-F Yen, B A Cheeseman				5c. PROGRAM ELEMENT NUMBER	
				622105	
				5d. PROJECT NUMBER	
				5e. TASK NUMBER	
				5f. WORK UNIT NUMBER	
7. PERFORMING ORGANIZATION NAMES AND ADDRESSES				8. PERFORMING ORGANIZATION REPORT NUMBER	
Clemson University Office of Sponsored Programs 300 Brackett Hall Clemson, SC 29634 -5702					
9. SPONSORING/MONITORING AGENCY NAME(S) AND ADDRESS(ES) U.S. Army Research Office P.O. Box 12211 Research Triangle Park, NC 27709-2211				10. SPONSOR/MONITOR'S ACRONYM(S) ARO	
				11. SPONSOR/MONITOR'S REPORT NUMBER(S) 57228-EG.1	
12. DISTRIBUTION AVAILABILITY STATEMENT Approved for public release; distribution is unlimited.					
13. SUPPLEMENTARY NOTES The views, opinions and/or findings contained in this report are those of the author(s) and should not be construed as an official Department of the Army position, policy or decision, unless so designated by other documentation.					
14. ABSTRACT Interactions between the rotating and advancing pin-shaped tool (terminated at one end with a circular-cylindrical shoulder) with the clamped welding plates and the associated material and heat transport during a friction-stir welding (FSW) process are studied computationally using a fully coupled thermomechanical finite element analysis. To surmount potential numerical problems associated with extensive mesh distortions/entanglement, an arbitrary					
15. SUBJECT TERMS fully coupled thermomechanical finite element analysis, friction-stir welding, welding plates, Lagrangian-Eulerian formulation					
16. SECURITY CLASSIFICATION OF:			17. LIMITATION OF ABSTRACT	15. NUMBER OF PAGES	19a. NAME OF RESPONSIBLE PERSON
a. REPORT	b. ABSTRACT	c. THIS PAGE			Mica Grujicic
UU	UU	UU	UU		19b. TELEPHONE NUMBER
					864-656-5639

Report Title

Fully coupled thermomechanical finite element analysis of material evolution during friction-stir welding of AA5083

ABSTRACT

Interactions between the rotating and advancing pin-shaped tool (terminated at one end with a circular–cylindrical shoulder) with the clamped welding plates and the associated material and heat transport during a friction-stir welding (FSW) process are studied computationally using a fully coupled thermomechanical finite element analysis. To surmount potential numerical problems associated with extensive mesh distortions/entanglement, an arbitrary Lagrangian–Eulerian (ALE) formulation was used, which enabled adaptive remeshing (to ensure the continuing presence of a high-quality mesh) while allowing full tracking of the material-free surfaces. To demonstrate the utility of the present computational approach, the analysis is applied to the case of FSW of AA5083 (a solid–solution strengthened and strainhardened/stabilized Al–Mg wrought alloy). To account for the competition between plastic deformation-controlled strengthening and dynamic recrystallization-induced softening phenomena during the FSW process, the original Johnson–Cook strain and strain-rate hardening and temperature-softening material strength model is modified using the available recrystallization kinetics experimental data. Lastly, the computational results obtained in the present work are compared with their experimental counterparts available in the open literature. This comparison revealed that general trends regarding spatial distribution and temporal evolutions of various material-state quantities and their dependence on the FSW process parameters are reasonably well predicted by the present computational approach.

REPORT DOCUMENTATION PAGE (SF298)
(Continuation Sheet)

Continuation for Block 13

ARO Report Number 57228.1-EG

Fully coupled thermomechanical finite element a ...

Block 13: Supplementary Note

© 2010 . Published in Proc. IMechE Part B: J. Engineering Manufacture, Vol. Ed. 0 224, (4) (2010), (, (4). DoD Components reserve a royalty-free, nonexclusive and irrevocable right to reproduce, publish, or otherwise use the work for Federal purposes, and to authorize others to do so (DODGARS §32.36). The views, opinions and/or findings contained in this report are those of the author(s) and should not be construed as an official Department of the Army position, policy or decision, unless so designated by other documentation.

Approved for public release; distribution is unlimited.

Fully coupled thermomechanical finite element analysis of material evolution during friction-stir welding of AA5083

M Grujicic^{1*}, T He¹, G Arakere¹, H V Yalavarthy¹, C-F Yen², and B A Cheeseman²

¹Department of Mechanical Engineering, Clemson University, Clemson, South Carolina, USA

²Army Research Laboratory, Aberdeen, Proving Ground, Maryland, USA

The manuscript was received on 28 July 2009 and was accepted after revision for publication on 3 September 2009.

DOI: 10.1243/09544054JEM1750

Abstract: Interactions between the rotating and advancing pin-shaped tool (terminated at one end with a circular-cylindrical shoulder) with the clamped welding plates and the associated material and heat transport during a friction-stir welding (FSW) process are studied computationally using a fully coupled thermomechanical finite element analysis. To surmount potential numerical problems associated with extensive mesh distortions/entanglement, an arbitrary Lagrangian–Eulerian (ALE) formulation was used, which enabled adaptive remeshing (to ensure the continuing presence of a high-quality mesh) while allowing full tracking of the material-free surfaces. To demonstrate the utility of the present computational approach, the analysis is applied to the case of FSW of AA5083 (a solid-solution strengthened and strain-hardened/stabilized Al–Mg wrought alloy). To account for the competition between plastic deformation-controlled strengthening and dynamic recrystallization-induced softening phenomena during the FSW process, the original Johnson–Cook strain and strain-rate hardening and temperature-softening material strength model is modified using the available recrystallization kinetics experimental data. Lastly, the computational results obtained in the present work are compared with their experimental counterparts available in the open literature. This comparison revealed that general trends regarding spatial distribution and temporal evolutions of various material-state quantities and their dependence on the FSW process parameters are reasonably well predicted by the present computational approach.

Keywords: fully coupled thermomechanical finite element analysis, friction-stir welding, welding plates, Lagrangian–Eulerian formulation

1 INTRODUCTION

Friction-stir welding (FSW) is a solid-state material that is generally employed in applications in which the original material microstructure/properties must remain unchanged as much as possible after joining [1–3]. In this process, as shown in Fig. 1(a), a rotating tool moves along the contacting surfaces of two rigidly butt-clamped plates. As seen in this figure, the tool consists of a cylindrical pin that is threaded, at one end, and equipped with a shoulder, at the other. Also, during joining, the workpiece (i.e. the two clamped

plates) is generally placed on a rigid backing support. At the same time, the shoulder is forced to make a firm contact with the top surface of the workpiece. As the tool (rotates and) moves along the butting surfaces, heat is being generated at the shoulder/workpiece and, to a lesser extent, at the pin/workpiece contact surfaces, as a result of the frictional energy dissipation. This, in turn, causes an increase in temperature and gives rise to softening of the material adjacent to these contacting surfaces. As the tool advances along the butting surfaces, thermally softened material in front of the tool is (heavily) deformed, transferred (i.e. extruded around the tool) to the region behind the tool and compacted/forged to form a joint/weld. It should be recognized that FSW can be used not only for butt joining but also for lap as well as T joints.

*Corresponding author: Department of Mechanical Engineering, Clemson University, 241 EIB, Clemson, SC 29634, USA. email: mica@ces.clemson.edu

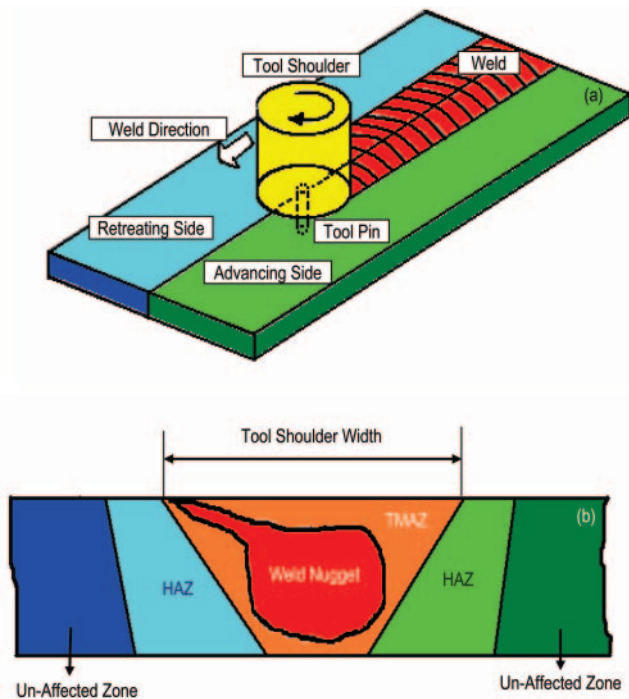


Fig. 1 (a) A schematic of the friction stir welding (FSW) process and (b) the main microstructural zones associated with the typical FSW joint

Since its discovery in 1991 [1], FSW has established itself as a preferred joining technique for aluminium components and its applications for joining other difficult-to-weld metals is gradually expanding. Currently, this joining process is being widely used in many industrial sectors such as shipbuilding and marine, aerospace, railway, land transportation, etc.

In comparison to the traditional fusion welding technologies, FSW offers a number of advantages, such as: (a) good mechanical properties in the *as-welded* condition; (b) improved safety due to the absence of toxic fumes or the spatter of molten material; (c) no requirement for consumables such as a filler metal or gas shield; (d) ease of process automation; (e) ability to operate in all positions (horizontal, vertical, overhead, orbital, etc.), as there is no weld pool; (f) minimal thickness under/over-matching, which reduces the need for expensive post-weld machining; and (g) low environmental impact. However, some disadvantages of the FSW process have also been identified, such as: (a) an exit hole is left after the tool is withdrawn from the workpiece; (b) relatively large tool press-down and plate-clamping forces are required; (c) lower flexibility of the process with respect to variable-thickness and non-linear welds; and (d) often associated with lower welding rates than conventional fusion-welding techniques, although this shortcoming is somewhat lessened since fewer welding passes are required.

When analysing the FSW process, a distinction is often made between the so-called *advancing* side of the weld (the side on which the peripheral velocity of the rotating tool coincides with the transverse velocity of the tool) and the *retreating* side (the side on which the two velocities are aligned in the opposite directions). It is generally recognized that the differences in the two weld sides give rise to asymmetry in heat transfer, material flow, and weld microstructure properties [4].

FSW normally involves complex interactions and competition between various thermomechanical processes such as friction–energy dissipation, plastic deformation and the associated heat dissipation, material transport/flow, dynamic recrystallization, local cooling, etc. [5–8]. Metallographic examinations of the FSW joints typically reveal the existence of the following four zones (Fig. 1(b)): (a) an unaffected zone, which is far enough from the weld so that material microstructure/properties are not altered by the joining process; (b) the heat affected zone (HAZ) in which material microstructure/properties are affected only by the thermal effects associated with FSW; while this zone is normally found in the case of fusion welds, the nature of the microstructural changes may be different in the FSW case due to generally lower temperatures and a more diffuse heat source; (c) the thermomechanically affected zone (TMAZ), which is located closer than the HAZ zone to the butting surfaces; consequently both the thermal and the mechanical aspects of the FSW affect the material microstructure/properties in this zone and, typically, the original grains are retained in this zone although they may have undergone severe plastic deformation; and (d) the weld *nugget*, which is the innermost zone of an FSW joint. As a result of the way the material is transported from the regions ahead of the tool to the wake regions behind the tool, this zone typically contains the so-called *onion ring* features. The material in this region has been subjected to the most severe conditions of plastic deformation and high-temperature exposure and consequently contains a very fine dynamically recrystallized (equiaxed grain) microstructure.

A unique feature of the FSW process is that heat transfer does not only take place via thermal conduction but also via transport of the workpiece material adjacent to the tool from the region in front to the region behind the advancing tool. In general both the heat and the mass transfers depend on the workpiece material properties, tool geometry, and the FSW process parameters. As mentioned earlier, mass transport is accompanied by extensive plastic deformation and dynamic recrystallization of the transported material. The attendant strain rates as high as 10/s have been assessed/measured [13, 14].

Q2

The main FSW process parameters that affect both the weld quality and the process efficiency are: (a) rotational and transverse velocities of the tool; (b) tool plunge depth; (c) tool tilt angle; and (d) tool design/material. Since, in general, higher temperatures are encountered in the case of higher rotational and lower transverse tool velocities, it is critical that a delicate balance between these two velocities is attained: i.e. when the temperatures are not high enough and the material has not been sufficiently softened, the weld zone may develop various flaws/defects arising from low ductility of the material. Conversely, when the temperatures are too high undesirable changes in the material microstructure/properties may take place and possibly incipient melting flaws may be created during joining. To ensure that the necessary level of shoulder/workpiece contact pressure is attained and that the tool fully penetrates the weld, the tool plunge depth (defined as the depth of the lowest point of the shoulder below the surface of the welded plate) has to be set correctly. Typically, insufficient tool plunge depths result in low-quality welds (due to inadequate forging of the material at the rear of the tool), while excessive tool plunge depths lead to undermatching of the weld thickness compared to the base material thickness. Tool rearward tilting by 2–4 degrees has been often found to be beneficial since it enhances the effect of the forging process.

Over the last two decades, considerable experimental research efforts have been invested towards providing a better understanding of the FSW joining mechanism and the accompanying evolution of the welded material's microstructure/properties (see, for example, references [15] to [18]) as well as to rationalizing the effect of various FSW process parameters on the weld quality/integrity (e.g. references [19] to [23]). It should be recognized, however, that the aforementioned experimental efforts were able to only correlate the postmortem welded material's properties/microstructure with the FSW process parameters and provided relatively little real-time insight into the physics of heat/mass transfer and microstructure evolution processes. It is hoped that this insight can be gained by carrying out detailed physically based computational investigations of the FSW process. An example of such an investigation is provided in the present manuscript.

A review of the public domain literature revealed a number of prior research efforts dealing with numerical investigations of the FSW process. For example, in a series of papers, Zhang and co-workers carried out a fairly comprehensive semi-coupled thermomechanical finite element investigation of the FSW process and the associated microstructural changes [29–31]. Similarly, a number of computational solid mechanics and

computational fluid dynamics investigations were reported in the literature whose main objective was to investigate the effect of various FSW process parameters (including tool design) on the heat/mass transport processes (e.g. references [29] to [33]).

The main objective of the present work is to carry out a detailed finite element computational investigation of the effect of various FSW process parameters on the heat and mass transport of the material and on the microstructure evolution for the case of the AA5083 wrought aluminium alloy. While similar investigations have been carried out by other researchers (e.g. references [29] to [31]), an effort is made in the present work to more accurately account for the competition between strain hardening and dynamic recrystallization processes in this alloy during FSW. In other words, while previous investigations recognized correctly the effect of plastic strain, strain rate, and temperature on the material strength, only reversible effects of the temperature were accounted for. This shortcoming was rectified in the present work by recognizing that, via dynamic recrystallization, exposure of the material to high temperatures may result in permanent microstructure/property changes.

The organization of the paper is as follows. In various subsections of section 2, details are provided regarding the basic formulation of the problem, fully coupled thermomechanical finite element analysis and its integration, workpiece material models, the tool/workpiece contact algorithm, and the arbitrary Lagrangian–Eulerian adaptive meshing method. The main results obtained in the present work are presented and discussed in section 3, while the key conclusions resulting from the present study are summarized in section 4.

2 COMPUTATIONAL PROCEDURE

2.1 Problem definition

As mentioned above, the main objective of the present work is to carry out a detailed finite element computational investigation of the FSW process. Since the purpose of the present investigation is to help establish the basic relationships between the key process parameters and the joined materials flow, a relatively simple workpiece and tool geometries are used (see the next section). Also, since FSW is generally used for joining aluminium alloys, a prototypical aluminium alloy/temper AA5083-H321 is used as the workpiece material. A fairly detailed description of this alloy and its H321-temper condition are provided later.

2.2 Geometrical and meshed models

The geometrical models for the workpiece and the tool are shown in Figs 2(a) and (b). For simplicity, the workpiece is considered as a single part; i.e. a *perfect clamping* condition is assumed. The workpiece is modelled as a circular solid plate with a radius of 40.0 mm and thickness of 3.0 mm. As will be clarified later, due to the use of an arbitrary Lagrangian–Eulerian (ALE) formulation, the circular plate displayed in Fig. 2(a) effectively represents a circular region surrounding the tool in an, otherwise, infinitely long FSW workpiece. The plate is considered to contain a concentric circular through-the-thickness hole with a radius of 3.0 mm. The two-part tool is modelled using a 3.0 mm radius cylindrical pin lower section and a 9.0 mm radius circular disc-shaped upper shoulder section. The bottom surface of the shoulder is not parallel with the workpiece but is rather inclined at an angle of 80.5 degrees (with respect to the vertical axis of the tool).

The workpiece is meshed using ~9000 first-order eight-node reduced-integration hexahedral thermo-mechanically coupled solid elements, while the tool was meshed using ~2000 first-order four-node reduced-integration rigid shell elements. Thermal properties of the tool are modelled using one single-node heat-capacity type of element. The meshed models for the workpiece and the tool are shown in Figs 3(a) and (b) respectively.

2.3 Fully coupled thermomechanical analysis

To investigate the FSW process, a fully coupled thermomechanical finite element analysis was utilized. Within this analysis, the nodal degrees of freedom

include both the nodal velocities and nodal temperatures. Furthermore, solid mechanics and heat-transfer aspects of the analysis are two-way/fully coupled; i.e. the work of plastic deformation and that associated with frictional sliding are considered as heat sources within the thermal analysis, while the effect of local temperature on the mechanical aspect of the analysis is accounted for through the use of temperature-dependent workpiece material properties.

At the beginning of the computational analysis, the following (initial) conditions are employed: the tool is assigned a fixed rotational speed in at a range of 200–400 r/min and a zero translational velocity, while the workpiece is assumed to be stationary. Both the tool and the workpiece are initially set to a temperature of 298 K.

During the analysis, the following boundary conditions are employed: (a) the bottom of the workpiece is constrained in the through-the-thickness direction; (b) the tool rotation is maintained at the same initial angular velocity; (c) a fixed contact pressure of 70 MPa is applied over the tool shoulder/workpiece contact interface; and (d) the workpiece is not translated along the weldline during the first 2 s. Thereafter, tool translation along the weldline is accomplished by applying a constant material flow velocity in the weldline direction over the *in-flow* and *out-flow* rim surfaces of the workpiece. Heat convection thermal boundary conditions are applied over the portions of the workpiece surfaces that are not in contact with the tool. Typical values for

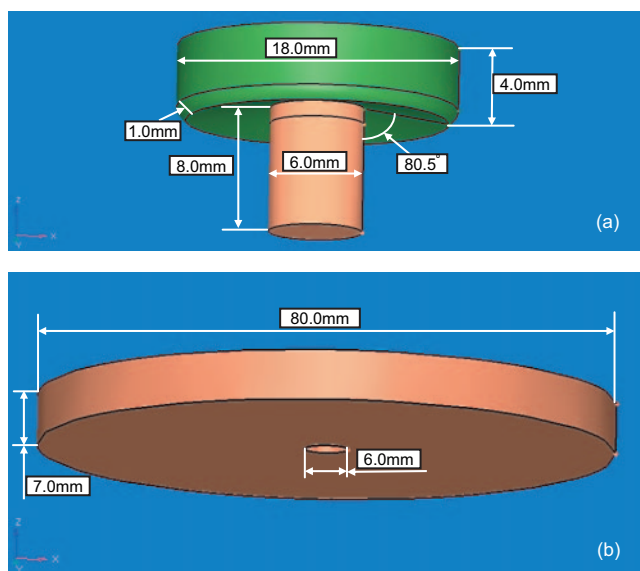


Fig. 2 Geometrical models with dimensions for (a) the FSW tool and (b) the FSW workpiece

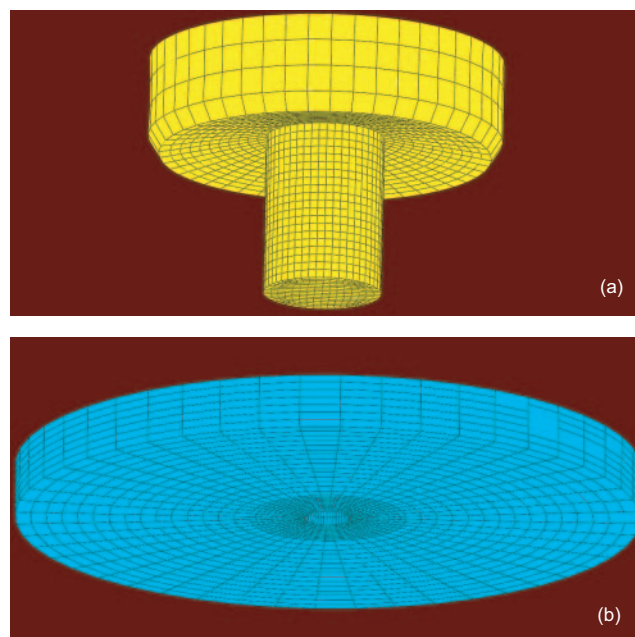


Fig. 3 Meshed models for (a) the FSW tool and (b) the FSW workpiece

the heat transfer coefficient are assigned to the workpiece/air and to the workpiece/backing plate interfaces.

To deal with the potential hourglassing problem associated with the use of reduced integration elements and the incompressible nature of plastic deformation in the workpiece material, a relaxed hourglass stiffness method was employed.

The tool and the workpiece are allowed to interact over their contact surfaces. Specifically, contacts between the bottom surface of the tool shoulder and the top surface of the workpiece as well as those between the outer surface of the pin and the workpiece hole were considered. Details regarding the contact algorithm used are provided in section 2.5.

All the calculations are carried out using the commercial finite element package ABAQUS/Explicit [34].

2.4 Material models

As mentioned earlier, the FSW tool is considered to be rigid and, hence, no mechanical properties (except for the density) had to be specified for its material. On the other hand, since the tool was acquiring a portion of the heat generated as a result of tool-workpiece interfacial slip, during the FSW process its thermal capacity had to be specified. Considering the fact that the tool is often made of a hot-worked tool steel such as AISI H13, temperature-invariant thermal properties and density of this material were used to compute the thermal capacity of the tool [35].

As mentioned earlier, the alloy whose FSW behaviour is analysed in the present work is AA5083-H321. While often age-hardened Al alloys (e.g. AA6061-T6) are friction-stir welded, the microstructure evolution of these alloys during FSW is expected to be substantially more complex due to the unstable nature of its precipitates (i.e. precipitates can undergo partial or complete dissolution during alloy exposure to high temperature and can reappear upon cooling in different morphologies and number densities, and even precipitates with different crystal structures may appear). AA5083 (nominal chemical composition: 4.5 wt% Mg, 0.25 wt% Cr, 0.75 wt% Mn) is an Mg/Mn solid-solution hardened alloy and, in addition, in its H321 temper state is cold work-hardened and stabilized (to obtain a needed level of ageing/over-ageing resistance). While Al₆Mn precipitates are present in this alloy, due to the aforementioned stabilizing heat treatment, they are relatively resistant to both dissolution and coarsening so that the precipitate portion of the material microstructure can be taken as mainly unchanged during FSW.

For the workpiece material, both thermal and mechanical properties had to be specified. Assuming

that the workpiece is made of an aluminium alloy AA5083, the following temperature-invariant and microstructure-invariant thermal properties were used: thermal conductivity, k , = 120 W/m K; specific heat, c_p , = 880 J/kg K; and density, ρ , = 2700 kg/m³.

The workpiece material is assumed to behave as an isotropic linear-elastic and a strain-rate sensitive, strain-hardenable, and (reversibly) thermally softenable plastic material. In this type of material, the mechanical response is described by the following three relations: (a) a *yield criterion*, i.e. a mathematical relation that defines the condition which must be satisfied for the onset (and continuation) of plastic deformation; (b) a *flow rule*, i.e. a relation that describes the rate of change of different plastic strain components during plastic deformation; and (c) a *constitutive law*, i.e. a relation that describes how the material strength changes as a function of the extent of plastic deformation, the rate of deformation, and temperature. For AA5083 analysed in the present work, the following specific mechanical model relations were used:

2.4.1 Yield condition

The von Mises yield condition was used, according to which the equivalent stress $\bar{\sigma}$ must be equal to the material yield strength, σ_y , i.e.

$$f(\sigma'_{ij}, \sigma_y) = \bar{\sigma} - \sigma_y = \sqrt{(3/2)\sigma'_{ij}\epsilon'_{ij}} - \sigma_y \geq 0 \quad (1)$$

where f is the yield function, σ'_{ij} and ϵ'_{ij} denote respectively the stress and strain components, the superscript ' is used to denote deviatoric quantities, and repeated subscripts imply summation.

2.4.2 Flow rule

The associative/normality flow rule is used in the present work, according to which the plastic flow takes place in the direction of the stress gradient of the yield surface as

$$\dot{\epsilon}^{pl} = \dot{\lambda} \frac{df}{d\sigma'_{ij}} \quad (2)$$

where the superscript ^{pl} is used to denote a plasticity-related quantity, a raised dot denotes a time derivative and $\dot{\lambda}$ is a proportionality constant.

2.4.3 Constitutive law

In the present work, the workpiece material yield strength was assumed to be controlled by strain and strain-rate hardening as well as by reversible thermally activated slip-controlled thermal softening effects. Accordingly, the Johnson-Cook strength model [36] was used as the basis for constitutive law in the material under investigation. This model is

capable of representing the material behaviour displayed under large-strain, high deformation rate, high-temperature conditions, of the type encountered in the problem of computational modelling of the FSW process. Within the Johnson–Cook model, the yield strength is defined as

$$\sigma_y = \left[A + B(\bar{\epsilon}^{pl})^n \right] \left[1 + C_1 \log(\dot{\bar{\epsilon}}^{pl}/\dot{\bar{\epsilon}}_0^{pl}) \right] \left[1 - T_H^m \right] \quad (3)$$

where $\bar{\epsilon}^{pl}$ is the equivalent plastic strain, $\dot{\bar{\epsilon}}^{pl}$ the equivalent plastic strain rate, $\dot{\bar{\epsilon}}_0^{pl}$ a reference equivalent plastic strain rate, A the zero-plastic-strain, unit-plastic-strain-rate, room-temperature yield strength, B the strain-hardening constant, n the strain-hardening exponent, C_1 the strain-rate constant, m the thermal-softening exponent, and $T_H = (T - T_{room}) / (T_{melt} - T_{room})$, a room-temperature (T_{room}) based homologous temperature while T_{melt} is the melting temperature. All temperatures are given in Kelvin. A summary of the Johnson–Cook strength model parameters for AA5083 is provided in Table 1.

While in the original Johnson–Cook strength model the evolution of the equivalent plastic strain is assumed to be controlled entirely by the plastic deformation process, in the present work, plastic strain evolution is assumed to be controlled by competition between plastic yielding and dynamic recrystallization. Since this represents one of the key contributions of the present work, details regarding the proposed modifications of the Johnson–Cook strength model are deferred to the results in the discussion section, section 3.

2.4.4 Integration of the stress state

During loading, the stress is updated by integrating the rate form of Hooke's law

$$\dot{\sigma}_{ij} = C_{ijkl} \dot{\epsilon}_{kl}^{el} = C_{ijkl} \dot{\epsilon}_{kl} - C_{ijkl} \dot{\epsilon}_{kl}^{pl} \quad (4)$$

where C_{ijkl} is the fourth-order elastic stiffness tensor and the total strain rate $\dot{\epsilon}$ is assumed to be comprised of its elastic, $\dot{\epsilon}^{el}$, and plastic, $\dot{\epsilon}^{pl}$, components. At each step during loading, the total strain rate is known (computed from the known velocity gradient).

Table 1 Johnson–Cook strength model material parameters for AA5083-H116

Parameter	Symbol	Units	Value
Reference strength	A	MPa	167.0
Strain-hardening parameter	B	MPa	596.0
Strain-hardening exponent	n	N/A	0.551
Strain-rate coefficient	C	N/A	0.001
Room temperature	T_{room}	K	293
Melting temperature	T_{melt}	K	893.0
Temperature exponent	m	N/A	1.0

After equation (2) is plugged into equation (4), equations (1) to (4) constitute a set of eight equations with eight unknowns ($\dot{\sigma}_{ij}$, $\dot{\lambda}$, σ_y). These equations can be readily solved/integrated using one of the numerical integration techniques.

2.5 Tool/workpiece interactions/contact

Normal interactions between the tool and the workpiece were accounted for using a *penalty* contact algorithm. Within this algorithm, the penetration of the surfaces into each other is resisted by linear spring forces/contact pressures with values proportional to the depth of penetration. These forces therefore tend to pull the surfaces into an equilibrium position with no penetration. Contact pressures between two bodies are not transmitted unless the nodes on the *slave surface* contact the *master surface*. There is no limit to the magnitude of the contact pressure that could be transmitted when the surfaces are in contact. Transmission of shear stresses across the contact interfaces is defined in terms of a static and a kinetic friction coefficient and a stick/slip critical shear stress level (the maximum value of shear stress that can be transmitted before the contacting surfaces begin to slide). In accordance with standard practice in this field, both the static and the kinetic friction coefficients are set to a value of 0.3. The stick/slip critical shear stress level is defined using a modified Coulomb friction law. Within this law, there is an upper limit of this quantity, which is equal to the shear strength of the softer of the two contacting materials. Thus at each level of the pressure, the stick/slip critical shear stress level is defined as the smaller of the following two shear stress values: (a) the softer material shear strength and (b) a product of the friction coefficient and the contact pressure. It should be recognized that both the contact pressure and the contact shear stress are computed as part of the complete FSW boundary-value problem.

Frictional slip/sliding at the tool/workpiece contact interfaces is considered as a potential heat source. The heat generated per unit contact surface area per unit time, q , is taken to scale with the magnitude of the tangential/interface shear stress, τ , and the slip rate, ds/dt , as

$$q = \eta \tau (ds/dt) \quad (5)$$

where η defines the fraction of the frictional slip energy that is converted to heat. The heat flux, q , is then partitioned between the tool and the workpiece. In the present work, it was assumed that the heat generated at the tool/workpiece interface is equally partitioned between the tool and the workpiece.

2.6 Explicit solution of the fully coupled thermomechanical problem

As mentioned earlier, to analyse the FSW process computationally, a fully coupled thermomechanical finite element analysis was employed. Within this analysis the thermal energy conservation equation in the form

$$\rho c_p \dot{T} = \nabla(k \nabla T) + \eta \sigma'_{ij} \dot{\epsilon}^{pl}_{ij} \quad (6)$$

and a (dynamic) mechanical equilibrium equation

$$\frac{\partial \sigma_{ij}}{\partial x_j} + f_i = \rho \frac{\partial^2 u_i}{\partial t^2} \quad (i, j = 1, 2, 3) \quad (7)$$

are solved, where ∇ is a gradient/divergence operator, x is the spatial coordinate, and f denotes a body force.

Within ABAQUS/Explicit, equation (7) is integrated using an explicit forward difference integration scheme as

$$T_{i+1} = T_i + \Delta t_{i+1} \dot{T}_i \quad (8)$$

where subscript i refers to the time-step increment number. The temperature rate vector, \dot{T}_i , is calculated at the end of the time increment i as

$$\dot{T}_i = C^{-1}(P_i - F_i) \quad (9)$$

where C^{-1} is the (inverse) lumped thermal capacity matrix, P the applied source vector, and F_i is the internal thermal flux vector.

The mechanical equilibrium equation is integrated using a central difference integration approach as

$$\dot{u}_{i+1/2} = \dot{u}_{i-1/2} + \frac{\Delta t_{i+1} + \Delta t_i}{2} \ddot{u}_i \quad (10)$$

$$\dot{u}_{i+1} = u_i + \Delta t_{i+1} \dot{u}_{i+1/2} \quad (11)$$

The acceleration vector at the end of the time increment i is computed as

$$\ddot{u}_i = M^{-1}(L_i - I_i) \quad (12)$$

where M^{-1} is the (inverse) mass matrix, L_i the applied load vector, and I_i is the internal force vector.

2.7 Computational cost

Computational investigations of manufacturing/fabrication processes such as FSW can be very costly/time consuming. This can particularly become an issue in the case of explicit finite element analyses, which are conditionally stable (i.e. these analyses entail that the time increment used be smaller than a critical/stable time increment). In the present fully coupled thermomechanical analysis both the mechanical and the thermal parts of the problem are associated with their respective stable time incre-

ments. The overall stable time increment is then defined as the smaller of the two.

The mechanical stable time increment is generally defined by the condition that, within the time increment, the stress wave must not propagate a distance longer than the minimal dimension of any finite element in the mesh. Consequently, the mechanical stable time increment is defined as $\Delta t_{\max, \text{mech}} = l_{\min}/c_d$, where l_{\min} is the smallest-element edge length, while c_d is the dilatational wave propagation velocity (sound speed), which is defined as $c_d = \sqrt{E/\rho}$, where E is Young's modulus. For aluminium alloys, the sound speed, c_d , is ca. 5100 m/s and for the smallest workpiece element size used in the present work (~ 0.6 mm), the stable time increment $\Delta t_{\max, \text{mech}}$ is $\sim 1.0 \times 10^{-7}$ s. For a typical FSW test runs of 20 s, an explicit finite element computational analysis would use $\sim 2 \times 10^8$ time increments. Using the computational facilities available for the present work, this would require an estimated computational wall time of 96 hours per single computational analysis. Since this computational cost was unacceptably high, a mass-scaling algorithm was used. Within this algorithm, material density is artificially increased in order to increase the stable time increment. The use of such a mass scaling algorithm does not alter the amount of heat generated by dissipation of plastic deformation work and frictional slip. Also, care was taken to ensure that a kinetic energy over internal energy ratio is less than 1 per cent, which is recommended in order to ensure that the mechanical portion of the solution is not altered by mass scaling.

The thermal stable time increment is generally defined by the condition that, within the time increment, the thermal wave must not propagate a distance longer than the minimal dimension of any finite element in the mesh. Consequently, the thermal stable time increment is defined as $\Delta t_{\max, \text{therm}} = l_{\min}^2/(2\alpha)$, where l_{\min} is the smallest-element edge length, while α is the thermal diffusivity. Using the aforementioned thermal property values for AA5083, the thermal stable time increment has been computed as $\Delta t_{\max, \text{therm}}$ is $\sim 1.0 \times 10^{-3}$ s. It should be noted that the mass scaling algorithm used does not affect this stable time increment and that the modified mechanical stable time increment does not exceed the thermal stable time increment. Consequently, mass scaling does not affect the thermal portion of the fully coupled thermomechanical problem investigated in the present work.

2.8 Arbitrary Lagrangian–Eulerian (ARL) formulation

As established earlier, FSW involves extensive plastic deformation and large-scale motion of the material from the region in front of the tool to the region

behind the tool. Under such conditions, the pure Lagrangian formulation in which the finite element mesh is attached to the material and moves/deforms with it can encounter serious numerical difficulties. To overcome this problem, the finite element analysis of the FSW process carried out in the present work was based on the so-called arbitrary Lagrangian–Eulerian (ALE) formulation. Within this algorithm, adaptive remeshing is carried out during a computational run to ensure that the mesh remains of a high quality. This approach is generally preferred over the pure Eulerian formulation in which the mesh remains unchanged/stationary while the material flows through it. Since the ALE mesh has a Lagrangian character, it can readily track material surfaces and prevent the formation of partially filled elements. The latter two problems are often cited as key shortcomings of the pure Eulerian formulation.

The ALE formulation used in the present work involved the following three main aspects:

- (a) The workpiece mesh is assumed to be stationary (i.e. of the Eulerian type) in the circumferential direction, while in the radial and in the through-the-thickness directions the same mesh is allowed to follow the material (i.e. the mesh is assumed to be of the Lagrangian type).
- (b) The *inflow* and *outflow* rim surfaces of the workpiece plate are treated as being pure Eulerian, and thus stationary.
- (c) The top and bottom workpiece plate surfaces are treated as being of the *sliding* type; i.e. the mesh is allowed to follow the material in the direction normal to the surface but remains stationary in the other two orthogonal directions.

3 RESULTS AND DISCUSSION

3.1 Material model modification to include the effects of dynamic recrystallization

As mentioned earlier, the workpiece material AA5083-H321 is modelled using a modified Johnson–Cook strain-hardening, strain-rate-sensitive, temperature-softening yield-strength model. Within the original Johnson–Cook model of equation (3), temperature provides only a reversible effect in promoting plastic deformation via thermal activation of dislocation glide and climb. Simply stated, higher temperatures promote plastic yielding but, per se, are not considered to (irreversibly) alter material microstructure/properties. However, as pointed out earlier, during FSW the workpiece material in the weld/stir zone becomes heavily plastically deformed and it is generally subjected to temperatures very near, yet lower than, the material melting tempera-

ture. Under these conditions, the material tends to undergo annealing at the same time as it is being deformed plastically. In other words, the material in the stir/nugget region tends to dynamically recrystallize, as a result of which the material strength/hardness (at high welding temperatures as well as at room temperature) is lowered relative to that in the base (H321 temper condition) material. This effect of temperature is not accounted for in the original Johnson–Cook model. Rather, only the effect of high temperatures on promoting plastic deformation via thermal activation is taken into account.

To overcome the aforementioned deficiency of the original Johnson–Cook model, a modification is proposed to the differential equation governing the evolution of the equivalent plastic strain. In the original Johnson–Cook model, this evolution was governed by simultaneously satisfying Hooke's law, yield criterion, and flow rule relations (see section 2.4). In this way, only the effect of strain hardening due to an increase in the dislocation density and the resulting increase in the dislocation motion resistance imposed by the surrounding dislocations is taken into account. To include the effects of dynamic recrystallization, a simple phenomenological-based relation for the additional (negative) component in the equivalent plastic strain rate is proposed. This equation is based on the following physics-based arguments:

- (a) Dynamic recrystallization is a thermally activated process and consequently the correction term in the equivalent plastic strain evolution equation must contain a Boltzmann probability term in the form $\exp(-Q/RT)$, where Q is an activation energy while R is the universal gas constant. In other words, the dynamic recrystallization correction to the Johnson–Cook strength model should be an Arrhenius-type function.
- (b) Since the rate of recrystallization across various alloy systems appears to scale with the dimensionless absolute-zero-based homologous temperature, T_h (defined as the ratio of the temperature and the melting temperature, both temperatures expressed in K), it is convenient to replace the Q/RT term in the Boltzmann probability relation with q/T_h , where q is a dimensionless activation energy.
- (c) Due to the fact that the rate at which material tends to recrystallize increases as the amount of cold work is increased, q should be a decreasing function of the equivalent plastic strain $\bar{\epsilon}_{pl}$.

Based on these arguments, the dynamic recrystallization contribution to the evolution of the equivalent plastic strain can be expressed as

$$\dot{\varepsilon}_{pl,dyn_rec} = \dot{\varepsilon}_{0,pl,dyn_rec} e^{(-q(\bar{\varepsilon}_{pl})/T_h)} \quad (13)$$

where $\dot{\varepsilon}_{0,pl,dyn_rec}$ is a dynamic recrystallization frequency/preexponential term. An analysis of the available experimental data pertaining to the kinetics of recrystallization of AA5083 [37] showed that q scales inversely with $\bar{\varepsilon}_{pl}$ raised to a power of 2.9. Based on this finding and using the curve-fitting results for the experimental recrystallization-kinetics data reported in reference [37], it is found that equation (13) can be rewritten as

$$\dot{\varepsilon}_{pl,dyn_rec} = 21.5e^{-1/(\bar{\varepsilon}_{pl}^{2.9} T_h)} \quad (14)$$

The effect of equation (14) on modifying the behaviour of AA5083 under simple uniaxial tensile conditions is displayed in Figs 4(a) to (c). In Fig. 4(a), it is seen that when T_h is relatively low ($T_h = 0.3$), the effects of dynamic recrystallization are small so that the material strain hardens. In sharp contrast, when T_h is relatively high ($T_h = 0.9$), the effect of dynamic recrystallization is dominant so that, despite extensive plastic deformation, the material undergoes pronounced strain softening (Fig. 4(b)). In Fig. 4(c), it is seen that when the effects of strain hardening and dynamic recrystallization are comparable, at the intermediate values of T_h ($T_h = 0.5$) no significant change in material strength takes place during plastic deformation.

The oscillating behaviour of material strength seen in Fig. 4(c) is a result of the competition and the interaction between strain hardening and dynamic recrystallization induced softening processes; i.e. softer material tends to harden at a high rate and, when the amount of plastic strain in the workpiece becomes sufficiently large, the rate of dynamic recrystallization becomes high enough to bring the strength down. This type of oscillating strength behaviour is often a signature of the undergoing dynamic recrystallization process.

It should be recognized that the kinetics of recrystallization is generally described using the so-called Johnson–Mehl–Avrami equation (e.g. reference [38]). Within this equation, the volume fraction of the material recrystallized, as a function of time, is given by a characteristic S-shaped curve, which starts from a non-zero annealing time (the incubation period), increases with a higher and higher slope, and, ultimately, the slope decreases as the volume fraction of the recrystallized material approaches unity (Fig. 5). The inner steepest part of this curve generally covers the major portion (80–90 per cent) of the range of the recrystallized material volume-fraction. Taking this fact into account, the simple model proposed here assumes that the entire recrystallized material volume-fraction versus time curve can be represented by its inner part and that this portion can be

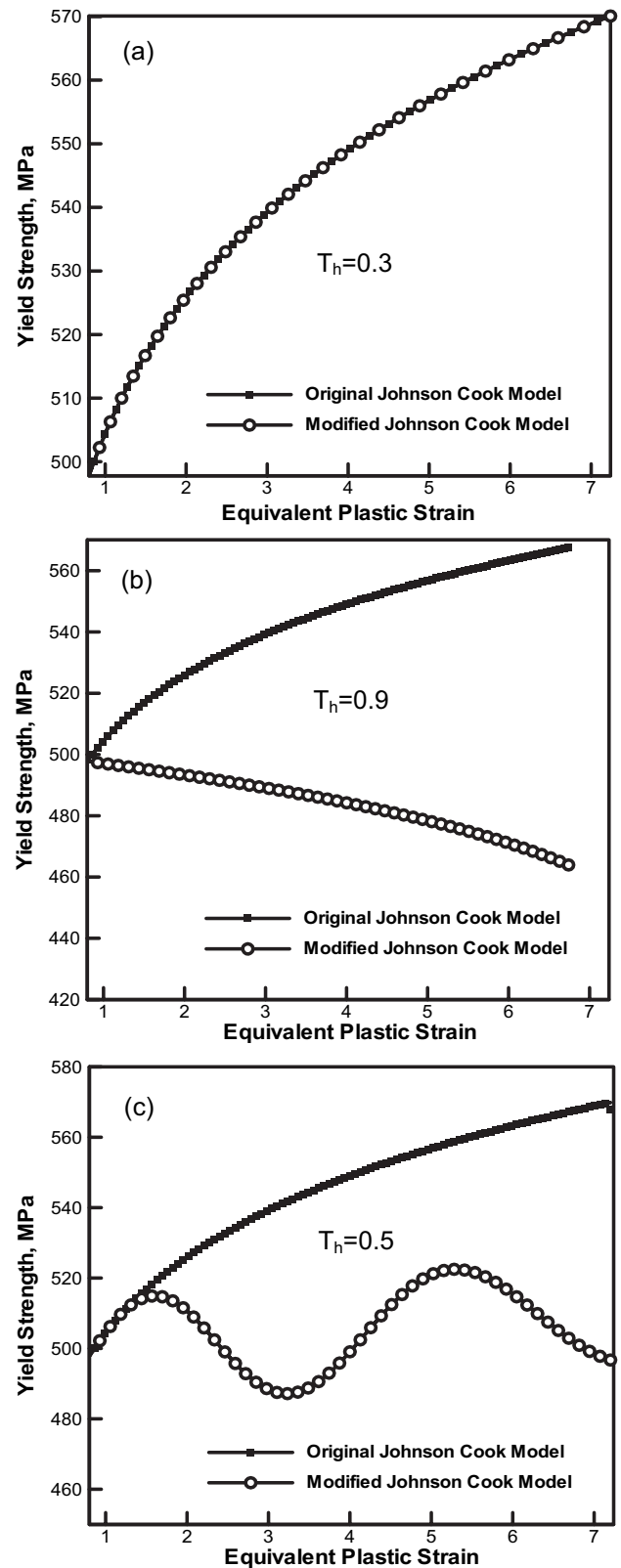


Fig. 4 A comparison of the strength versus equivalent plastic strain curves as predicted by the original and the modified Johnson–Cook strength models. The results are obtained under the uniaxial strain rate of 0.001/s and at three different homologous temperatures: (a) $\theta = 0.3$; (b) $\theta = 0.9$; (c) $\theta = 0.5$

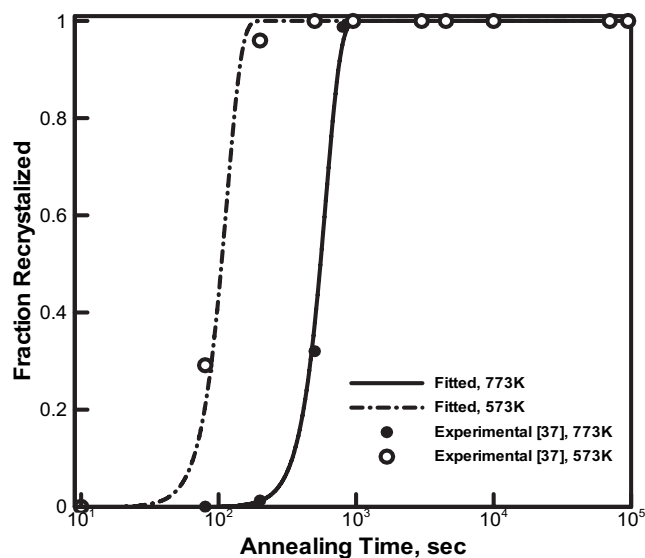


Fig. 5 Experimental results [37] and the fitting curves pertaining to the recrystallization kinetics in AA5083

linearized. The slope of this new linear function, on the other hand, is taken to be a function of the temperature and the equivalent plastic strain. Equation (14) is then obtained by assuming that $\dot{\epsilon}_{pl,dyn-rec}$ scales linearly with the rate of recrystallization.

To include the effects of dynamic recrystallization of the workpiece material on the material evolution during FSW, the modified Johnson–Cook material model is implemented into a user material subroutine *VUMAT:for* and linked with the ABAQUS/Explicit finite element solver. To validate the implementation of the material model, several FSW cases were analysed. It is found that when the effects of dynamic recrystallization are suppressed, the results (not shown for brevity), based on the user material model and the Johnson–Cook model (built in ABAQUS/Explicit) are essentially identical.

3.2 Typical computational results

In this section, examples of typical results obtained in the fully coupled finite element investigation of the FSW process carried out in this work are presented and discussed. The finite element analysis used allowed investigation of the effect of all the key FSW process parameters on the temporal evolution and spatial distribution of various material-related quantities such as: temperature, stress and strain components, equivalent plastic strain, local material strength, material velocity, trajectory of tracer particles that reveal temporal-dependent locations of the associated material particles as they are passing through the circular region surrounding the rotating pin tool, etc. Since similar results were shown and discussed in a series of papers by Zhang *et al.* [29–31],

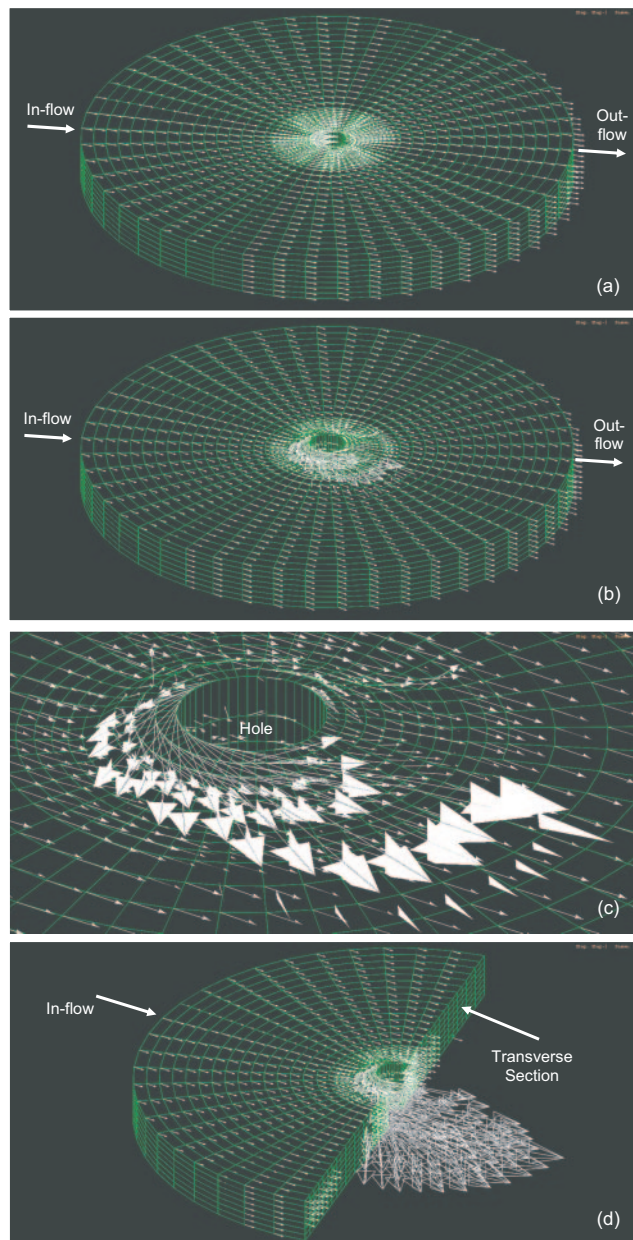


Fig. 6 A typical nodal-velocity field associated with friction stir welding: (a) the initial state; (b) the fully developed state; (c) a close-up of part (b); and (d) a close-up of the transverse section of part (b)

only a few representative and unique results will be displayed and discussed in this section.

3.2.1 Nodal velocity field

The distribution of nodal velocities at the outer surfaces of the workpiece at two different times (0.0 and 0.5 s) is displayed in Figs 6(a) and (b). For clarity, the tool is not shown in Figs 6(a) and (b), as well as in several other figures presented in the remainder of this document. These figures clearly show that the initially assigned unidirectional velocity field in the

direction of welding quickly transforms into the velocity field in which there is a well-defined stir region right below the shoulder (within which the material circles around the pin) and the remainder of the field (within which the material tends to flow around the stir region). A comparison of the results displayed in Figs 6(a) and (b) clearly shows how the region underneath the tool shoulder, which is initially unfilled, becomes filled as FSW proceeds (please note an increase in the workpiece hole upper rim altitude). Once the space under the shoulder is fully filled it remains filled as the FSW process continues. The material in this region is constantly being refreshed as the tool advances in the welding direction. To reveal the character of the nodal velocity field around the workpiece hole better, a close-up of this region is provided in Fig. 6(c). Furthermore, to reveal the tool-induced material stirring effect through the workpiece thickness, a transverse section of the plate is provided in Fig. 6(d).

3.2.2 Material/tracer particle trajectories

The results displayed in Figs 6(a) and (b) show the spatial distribution and temporal evolution of the nodal velocities. It should be noted that due to the ALE character of the finite element analysis used in the present work, the motion of the finite element mesh is not completely tied to the motion of the material. Thus the results displayed in Figs 6(a) and (b) show the velocities of the material particles, which at that moment pass through the nodal points. However, at different times different material particles are associated with the same nodes. To observe material extrusion around the tool pin and its forging at the tool wake, it is more appropriate to construct and analyse material particle trajectories. This is possible within ABAQUS/Explicit through the use of so-called *tracer particles*, which are attached to the material points (and not to the mesh nodal points).

An example of the prototypical results pertaining to the trajectory of retreating-side and advancing-side tracer particles is displayed in Figs 7(a) and (b) respectively. The tracer particles displayed in these figures are initially located in a plane that is halfway between the top and bottom surfaces of the workpiece. For improved clarity, tracer particle trajectories are colour coded. The results displayed in Figs 7(a) and (b) clearly revealed the following basic aspects of the FSW process:

- The workpiece material at the retreating side (as represented by the yellow and green tracer particle trajectories in Fig. 7(a)), does not, for the most part, enter the stir zone under the tool shoulder and usually only flows around it.
- The material at the advancing side (as represented by the white and cyan tracer particle

trajectories in Fig. 7(b)), which is initially close to the butting surfaces, passes over to the retreating side and is co-stirred with some of the retreating-side material to form the welded joint.

- The advancing-side material further away from the initial butting surfaces remains on the advancing side and either enters the stir region on the advancing side or flows around it.

3.2.3 Temperature field

A typical spatial distribution of temperature in the workpiece during FSW is displayed in Figs 8(a) and (b). The results displayed in Figs 8(a) and (b) refer to the temperature distributions over the medial longitudinal and medial transverse sections respectively. Simple examination of the results displayed in these figures and of the results obtained in the present work (but not shown for brevity) reveals that:

- Depending on the FSW process conditions such as tool contact pressure, tool rotational and translational speeds, temperatures in a range between 350 and 450 °C are obtained.
- The highest temperatures are always found in the workpiece material right below the tool shoulder and the temperatures progressively decrease from this region as a function of the distance in the radial and through-the-thickness directions.
- As the tool rotational speed and contact pressure are increased, higher temperatures are observed and temperature differences between the top and bottom surfaces of the workpiece are reduced.

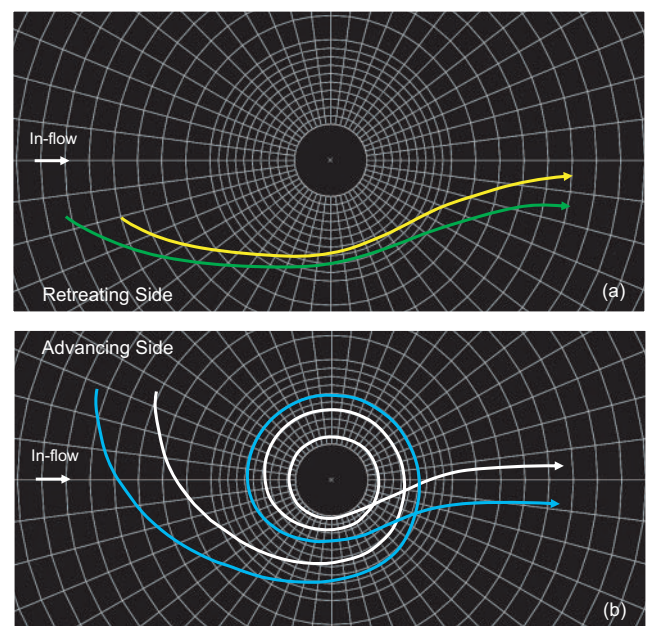


Fig. 7 (a) Retreating-side and (b) advancing-side tracer particle typical trajectories

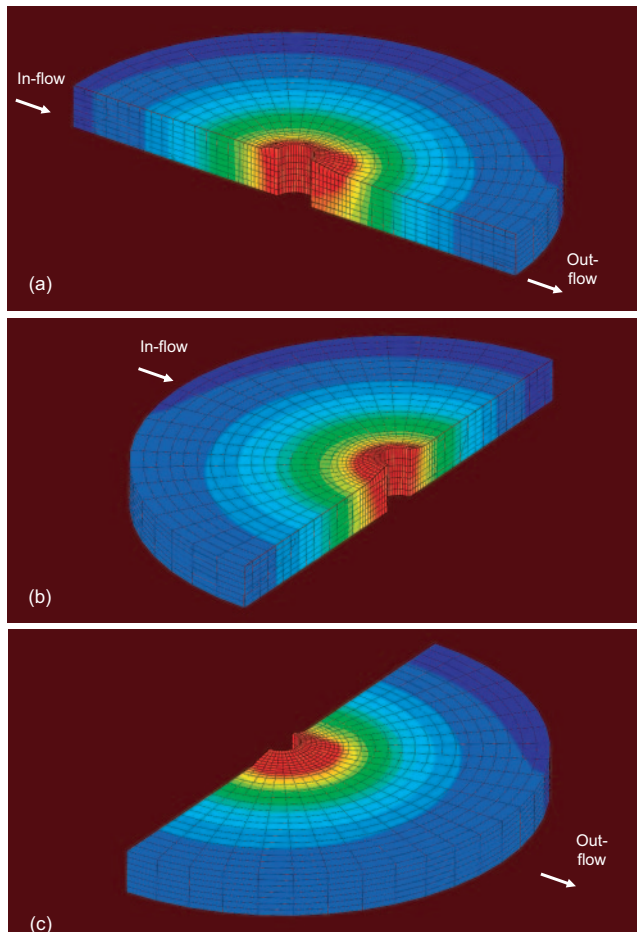


Fig. 8 Typical temperature distribution over one-half of the workpiece obtained by cutting along (a) the longitudinal and (b), (c) transverse directions: maximum (red) = 400 °C; minimum (blue) = 25 °C

- (d) By computing the energies dissipated via the plastic deformation process and those dissipated through frictional sliding at the tool/workpiece interfaces, it is found that plastic deformation typically contributes around 30 per cent to the overall heat generation and that this contribution increases slowly with an increase in the translational velocity of the tool.

3.2.4 Equivalent plastic strain field

A typical spatial distribution of equivalent plastic strain in the workpiece during FSW is displayed in Figs 9(a) and (b). The results displayed in Figs 9(a) and (b) refer to the equivalent plastic strain distributions over the medial longitudinal and medial transverse sections respectively. Simple examination of the results displayed in these figures and of the results obtained in the present work (but not shown for brevity) reveals that:

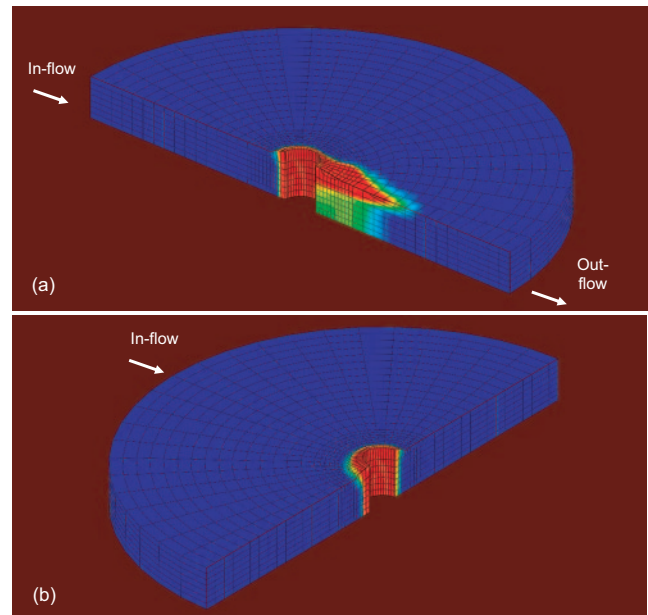


Fig. 9 Typical equivalent plastic strain distribution over one-half of the workpiece obtained by cutting along (a) the longitudinal and (b) transverse directions: maximum (red) = 120; minimum (blue) = 0

- (a) Depending on the FSW process conditions, such as tool contact pressure, tool rotational and translational speeds, equivalent plastic strains in a range between 100 and 150 are observed. This range of equivalent plastic strains is in general agreement with the ones previously reported by Zhang and co-workers (e.g. references [17] and [27] to [31]). It should be noted that the workpiece material is capable of undergoing such a large amount of plastic deformation due to the attendant high-pressure conditions. Such high-pressure conditions are normally not present in standard laboratory mechanical tests (e.g. uniaxial tension, compression, simple shear, etc.), which are used to parameterize the workpiece material model. Consequently, the results obtained in these tests reflect the material behaviour under significantly lower levels of the plastic strain and, as is generally done, it is assumed here that the established material model identification can be extrapolated into the extremely large equivalent plastic-strain range encountered in the FSW process.
- (b) The highest equivalent plastic strains are always found in the workpiece material right below the tool shoulder and equivalent plastic strains progressively decreased from this region as a function of the distance in the radial and through-the-thickness directions.
- (c) There is a highly pronounced asymmetry in the distribution of the equivalent plastic strain relative to the initial location of the butting surfaces.

This asymmetry is related to the aforementioned differences in the material transport (at the advancing and the retreating sides of the weld) from the region ahead of the tool to the region behind the tool.

- (d) As the tool translational speed is decreased and the tool/workpiece contact pressure is increased, higher equivalent plastic strains are observed and equivalent plastic strain differences between the top and bottom surfaces of the workpiece are reduced. This finding suggests that under these FSW process conditions the extent of material stirring/mixing (which plays a critical role in weld quality/joint strength) is increased.

3.2.5 Residual stress field

It is well established that friction-stir welded components contain significant levels of residual stresses, both in the direction of welding (the longitudinal direction) and in the direction normal to it (the transverse direction). These residual stresses are caused by non-uniform distributions in the extent of plastic deformations (as represented by the equivalent plastic strains) and in the temperature in different regions within the weld joint. Since the presence of residual stresses can significantly affect the structural and environmental resistance/durability of welded joints, it is critical that they are quantified and that their magnitudes and spatial distributions be correlated with various FSW process parameters. While a comprehensive investigation of the residual stress distribution as a function of the FSW process parameters is beyond the scope of the present work, an effort was invested here to develop computational capabilities for such investigations. Towards that end, the results of the FSW simulation are imported into the implicit finite element program ABAQUS/Standard and a quasi-static fully coupled thermomechanical analysis is carried out. It should be noted that ABAQUS/Explicit is not suitable for this type of investigation since it requires prohibitively long computational times. Within the quasi-static fully coupled thermomechanical analysis employed, the FSW tool is removed and the boundary conditions are eliminated from the workpiece while the temperature is progressively decreased down to room temperature.

An example of the results pertaining to the distribution of von Mises residual stresses over a medial longitudinal and transverse sections of the workpiece are displayed in Figs 10(a) and (b) respectively. Simple examination of the results displayed in these figures and of the results obtained in the present work (but not shown for brevity) reveals that:

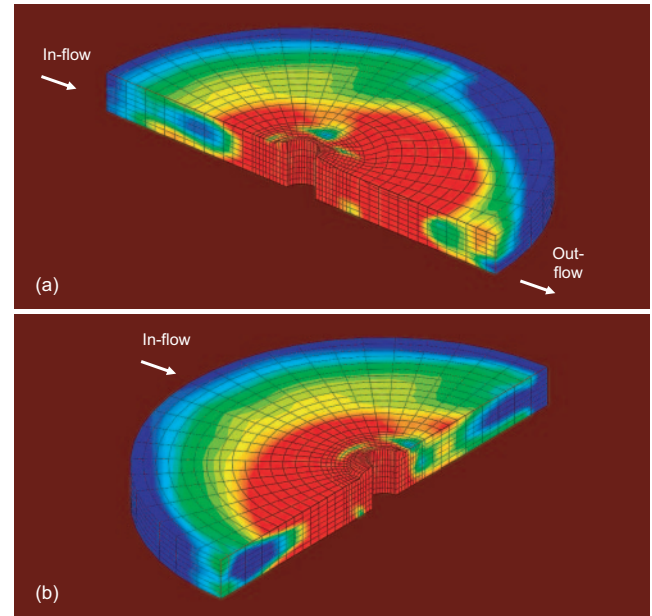


Fig. 10 Typical von Mises residual stress distribution over one-half of the workpiece obtained by cutting along (a) the longitudinal and (b) transverse directions: maximum (red) = 50 MPa; minimum (blue) = -20 MPa

- Maximum longitudinal residual stresses are generally higher than their maximum transverse counterparts by a factor of roughly two
- The residual stresses typically increase in magnitude as the distance from the initial portion of butting surfaces is reduced. However, in the innermost portion of the nugget, they tend to decrease somewhat. This is clearly related to the effect of dynamic recrystallization, which is prevalent in this region.
- Both the longitudinal and transverse residual stresses tend to increase with an increase in the tool rotational and translational velocities.

3.3 Comparison with experimental results

The results presented in the previous section (as well as the results obtained in the present work but not shown) are very reasonable and in good qualitative agreement with the general experimental observations/findings. However, if the computational approach like the one developed here is to become an integral part of the FSW practice and helps guide further development and optimization of this metal joining process, it must also demonstrate the needed level of quantitative agreement with the experimental results/observations. To assess the ability of the present computational approach to account for the experimentally measured FSW-related results, selected computational results are compared with their experimental counterparts obtained in the work of

Peel *et al.* [26]. The work carried out in reference [26] is quite comprehensive and thorough and involves AA5083, the aluminium alloy investigated in the present work. While the work of Peel *et al.* [26] yielded numerous results, only the following two types of these results could be directly compared with the finite element based computational results obtained in the present work: (a) variation of the longitudinal and transverse (normal) residual stresses as a function of the distance from the weldline and (b) variation of the room temperature material strength as a function of the distance from the weldline.

3.3.1 Residual stress distribution

A comparison between the present computed and the experimentally measured results reported in reference [26] pertaining to variation of the longitudinal and transverse residual stresses as a function of the distance from the initial location of the butting surfaces is displayed in Figs 11(a) and (b). Two sets of computational results are displayed in each case, one using the original Johnson–Cook model and the other using the modified Johnson–Cook model. This helped establish the extent of improvement in the material model formulation attained in the present work. Simple examination of the results displayed in Figs 11(a) and (b) reveals that the results obtained using the modified Johnson–Cook model is in significantly better agreement (than the original Johnson–Cook-based results) with the experimental results, making the overall computation/experiment agreement quite good. Specifically:

- The residual stresses are compressive at larger distances from the weldline at the advancing side of the weld (the right-hand side in Figs 11(a) and (b)).
- As the weldline at the advancing side is approached, the residual stresses first increase in magnitude and then switch their character (i.e. become tensile), at a distance of 15–20 mm from the weldline (at the advancing side).
- In the innermost portion of the nugget, the tensile residual stresses tend to decrease somewhat.
- As the distance from the weldline increases on the retreating side, the stresses gradually decrease towards zero.
- The longitudinal residual stresses are generally higher than their transverse counterparts.

3.3.2 Room-temperature material strength distribution

A comparison between the present computed results (as predicted by the modified and the original Johnson–Cook strength model) and the experimentally measured results reported in reference [26] pertain-

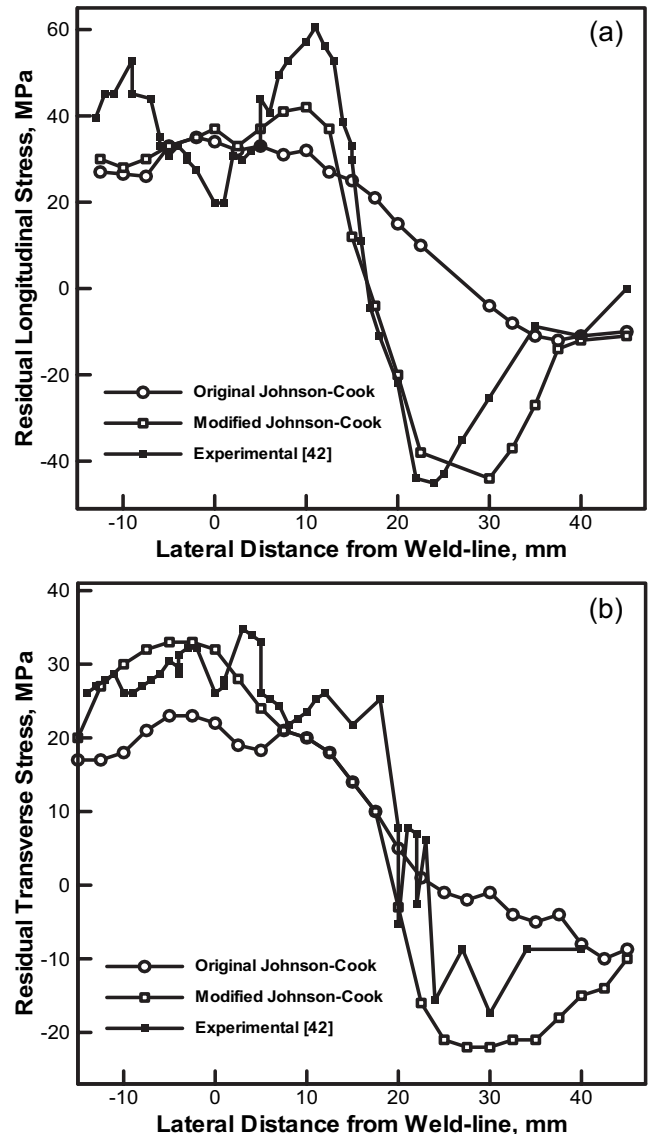


Fig. 11 Variation of (a) the longitudinal and (b) transverse residual stresses as a function of the distance from the weldline. Data pertaining to the advancing side of the weld joint are on the right-hand side of the plot

ing to variation of the room temperature material strength as a function of the distance from the initial location of the butting surfaces is displayed in Fig. 12. The results displayed in this figure show that, while the quantitative agreement between the computed and the experimental results is only fair, the present computed analysis correctly predicts the overall trend. This is quite encouraging considering the fact that the original Johnson–Cook strength model (in which the effect of dynamic recrystallization is neglected) incorrectly predicts that the highest room temperature strength levels are located in the innermost region of the nugget zone (where the equivalent plastic strain levels are also the highest).

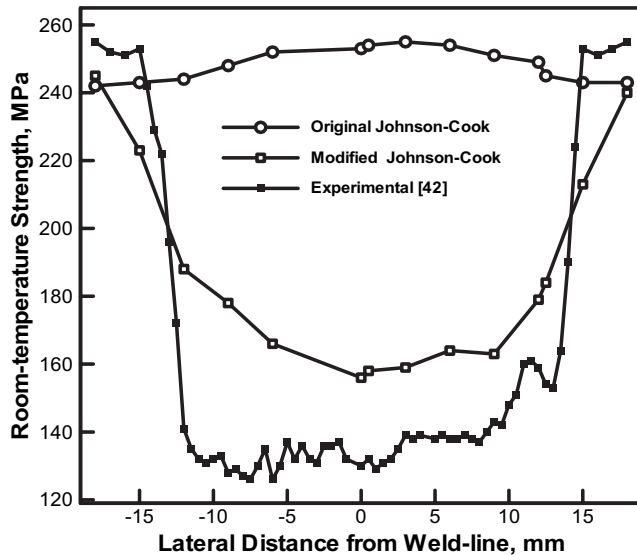


Fig. 12 Variation of the room-temperature material strength as a function of the distance from the weldline. Data pertaining to the advancing side of the weld joint are on the right-hand side of the plot

3.3.3 Material microstructure evolution

In the previous two sections, spatial variations within the FSW joint, in the residual stresses, and in the material strength were computed and compared with their experimental counterparts obtained in reference [26]. The material strength results were obtained by substituting the effective (i.e. dynamic-recrystallization modified) equivalent plastic strain in the Johnson–Cook strength model of equation (3). Within this approach, contributions of various microstructural features/processes (e.g. grain size, dislocation density, dispersoid number density, etc.) were lumped into a single parameter, the effective equivalent plastic strain. In ongoing work, an effort is made to identify and quantify separately the contributors to material strength (primarily the effect of grain size refinement and dislocation density-controlled strain hardening). In the approach used, separate evolution equations are being developed for both the grain size and the dislocation density, and the standing Hall–Petch grain-size-based strengthening [38] and Cocks, Argon, and Ashby strain-hardening models [39] are being utilized. An example of the preliminary results obtained in this investigation is displayed in Fig. 13, in which variation of the grain size as a function of the distance from the weld centre-line are displayed. These results are highly encouraging since they show a recrystallized fine-grain microstructure in the nugget zone and a somewhat coarser grain microstructure in the heat-affected zone (HAZ), which is consistent with the

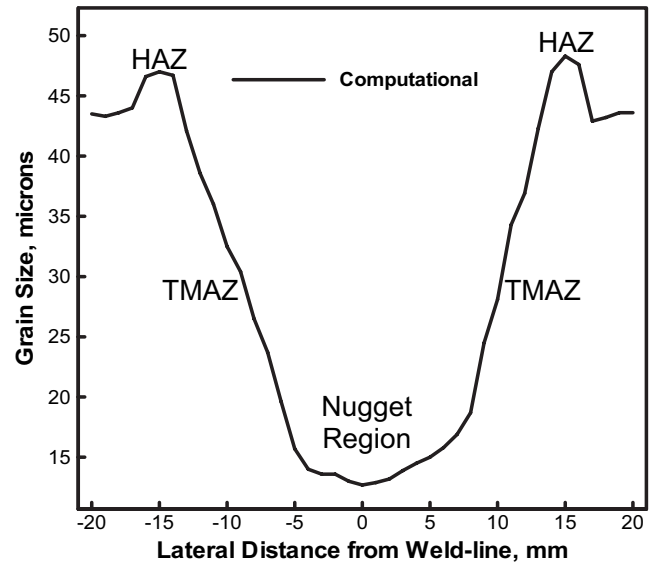


Fig. 13 Spatial variation of the grain size throughout the FSW joint as obtained computationally in ongoing work

typical findings made in the microstructural investigation of the FSW joints (e.g. reference [26]).

4 CONCLUSIONS

Based on the work presented and discussed in the present work, the following main summary remarks and conclusions can be made:

1. A comprehensive fully coupled thermo-mechanical finite element computational investigation of friction stir welding (FSW) of a prototypical solid-solution strengthened and strain-hardened aluminium alloy (AA5083) is carried out.
2. To model the microstructure/property evolution of this material during the FSW process, the original Johnson–Cook strength model is modified in order to account for the effects of dynamic recrystallization and the associated material softening taking place in the stir zone of the welded joint.
3. Various results obtained showed good overall qualitative agreement with the corresponding empirical findings/observations.
4. Limited quantitative experimental results pertaining to the variations of the longitudinal and transverse residual stresses with distance from the weldline and the associated variations in material strength are used to validate the modified Johnson–Cook finite element procedure employed. A reasonably good agreement is obtained between the computed and experimental results, suggesting that the modelling and simulation procedures used are adequate.

ACKNOWLEDGEMENTS

The material presented in this paper is based on work supported by the US Army/Clemson University Cooperative Agreements W911NF-04-2-0024 and W911NF-06-2-0042.

© Authors 2010

REFERENCES

- 1 Thomas, W. M., Nicholas, E. D., Needham, J. C., Murch, M. G., Temple-Smith, P., and Dawes, C. J. Friction stir butt welding, International Patent Application PCT/GB92/02203, 1991.
- 2 Dawes, C. J. and Thomas, W. M. Friction stir process welds aluminum alloys. *Welding J.*, 1996, **75**, 41–52.
- 3 Thomas, W. M. and Dolby, R. E. Friction stir welding developments. In *Proceedings of the Sixth International Conference on Trends in Welding Research* (Eds S. A. David, T. DebRoy, J. C. Lippold, H. B. Smartt, and J. M. Vitek), 2003, pp. 203–211 (ASM International, Materials Park, Ohio).
- 4 Cho, J. H., Boyce, D. E., and Dawson, P. R. Modeling strain hardening and texture evolution in friction stir welding of stainless steel. *Mater. Sci. Engng A*, 2005, **398**, 146–163.
- 5 Liu, H., Fulii, H., Maeda, M., and Nogi, K. Tensile properties and Fracture locations of friction-stir welded joints of 6061-T6 aluminium Alloy. *J. Mater. Sci. Lett.*, 2003, **22**, 1061–1063.
- 6 Lee, W. B., Lee, C. Y., Chang, W. S., Yeon, Y. M., and Jung, S. B. Microstructural investigation of friction stir welded pure titanium. *Mater. Lett.*, 2005, **59**, 3315–3318.
- 7 Thomas, W. M. and Nicholas, E. D. Friction stir welding for the transportation industries. *Mater. Des.*, 1997, **18**, 269–273.
- 8 Su, J. Q., Nelson, T. W., Mishra, R., and Mahoney, M. Microstructural investigation of friction stir welded 7050-T651 aluminum. *Acta Mater.*, 2003, **51**, 713–729.
- 9 Frigaard, O., Grong, Ø., and Midling, O. T. A process model for friction stir welding of age hardening aluminum alloys. *Metall. Mater. Trans. A*, 2001, **32**, 1189–1200.
- 10 Mahoney, M. W., Rhodes, C. G., Flintoff, J. G., Spurling, R. A., and Bingel, W. H. Properties of friction-stir-welded 7075 T651 aluminum. *Metall. Mater. Trans. A*, 1998, **29**, 1955–1964.
- 11 Rhodes, C. G., Mahoney, M. W., Bingel, W. H., Spurling, R. A., and Bampton, C. C. Effect of friction stir welding on microstructure of 7075 aluminum. *Scripta Mater.*, 1997, **36**, 69–75.
- 12 Liu, G., Murr, L. E., Niou, C. S., McClure, J. C., and Vega, F. R. Microstructural aspects of the friction-stir-welding of 6061-T6 aluminum. *Scripta Mater.*, 1997, **37**, 355–361.
- 13 Jata, K. V. and Semiatin, S. L. Continuous dynamic recrystallization during friction stir welding. *Scripta Mater.*, 2000, **43**, 743–748.
- 14 Masaki, K., Sato, Y. S., Maeda, M., and Kokawa, H. Experimental simulation of recrystallized microstructure in friction stir welded Al alloy using a plane-strain compression test. *Scripta Mater.*, 2008, **58**, 355–360.
- 15 Thomas, W. M., Nicholas, E. D., Needham, J. C., Murch, M. G., Temple-Smith, P., and Dawes, C. J. Friction stir welding. International Patent Application PCT/GB92102203 and Great Britain Patent Application 9125978.8, 1991.
- 16 Mishra, R. S. and Ma, Z. Y. Friction stir welding and processing. *Mater. Sci. Engng Rep.*, 2005, **50**, 1–78.
- 17 Zhang, H. W., Zhang, Z., and Chen, J. T. The finite element simulation of the friction stir welding process. *Mater. Sci. Engng A*, 2005, **403**, 340–348.
- 18 Ramirez, A. J. and Juhas, M. C. Microstructural evolution in Ti-6Al-4V friction stir welds. *Mater. Sci. Forum*, 2003, 426–432.
- 19 Su, J. Q., Nelson, T. W., Mishra, R., and Mahoney, M. Microstructural investigation of friction stir welded 7050-T651 aluminium. *Acta Mater.*, 2003, **51**, 713–729.
- 20 Salem, H. G., Reynolds, A. P., and Lyons, J. S. Microstructure and retention of superplasticity of friction stir welded superplastic 2095 sheet. *Scripta Mater.*, 2002, **46**, 337–342.
- 21 Liu, H. J., Chen, Y. C., and Feng, J. C. Effect of zigzag line on the mechanical properties of Friction Stir Welded Joints of an Al-Cu Alloy. *Scripta Mater.*, 2006, **55**, 231–234.
- 22 Ma, Z. Y., Sharma, S. R., and Mishra, R. S. Effect of friction stir processing on the microstructure of cast A356 aluminum. *Mater. Sci. Engng A*, 2006, **433**, 269–278.
- 23 Cavaliere, P., Campanile, G., Panella, F., and Squillace, A. Effect of welding parameters on mechanical and microstructural properties of AA6056 joints produced by friction stir welding. *J. Mater. Process. Technol.*, 2006, **180**, 263–270.
- 24 Cavaliere, P., Squillace, A., and Panella, F. Effect of welding parameters on mechanical and microstructural properties of AA6082 joints produced by friction stir welding. *J. Mater. Process. Technol.*, 2008, **200**, 364–372.
- 25 Elangovan, K. and Balasubramanian, V. Influences of tool pin profile and welding speed on the formation of friction stir processing zone in AA2219 aluminium alloy. *J. Mater. Process. Technol.*, 2008, **200**, 163–175.
- 26 Peel, M., Steuwer, A., Preuss, M., and Withers, P. J. Microstructure, mechanical properties and residual stresses as a function of welding speed in aluminium AA5083 friction stir welds. *Acta Mater.*, 2003, **51**, 4791–4801.
- 27 Zhang, H. W., Zhang, Z., and Chen, J. T. 3D Modeling of material flow in friction stir welding under different process parameters. *J. Mater. Process. Technol.*, 2007, **183**, 62–70.
- 28 Zhang, Z., Chen, J. T., and Zhang, H. W. The 3D simulation of friction stir welding process. In *International Conference on Mechanical engineering and mechanics* (Eds R. C. Batra, L. F. Qian, Y. L. Zhang, X. N. Li, and S. K. Tso), Nanjing, People's Republic of China, 2005, pp. 1388–1342.
- 29 Zhang, H. W. and Zhang, Z. Numerical modeling of friction stir welding process by using rate-dependent

- constitutive model. *J. Mater. Sci. Technol.*, 2007, **23**, 73–80.
- 30 Zhang, H. W., Zhang, Z., Bie, J., Zhou, L., and Chen, J. T.** Effect of viscosity on material behaviors in friction stir welding process. *Trans. Nonferr. Metal Soc. China*, 2006, **16**, 1045–1052.
- 31 Zhang, H. W. and Zhang, Z.** Numerical simulation of friction stir welding by using semi-coupled model. In *International Conference on Enhancement and promotion of computational methods in engineering science and mechanics* (Eds P. Hu and J. N. Reddy), Changchun, China, 10–12 August 2006, pp. 52–62.
- 32 Deng, X. M. and Xu, S. W.** Two-dimensional finite element simulation of material flow in friction stir welding process. *J. Manuf. Process.*, 2004, **6**, 125–133.
- 33 Xu, S., Deng, X., Reynolds, A. P., and Seidel, T. U.** Finite element simulation of material flow in friction stir welding. *Sci. Technol. Weld Joint*, 2001, **6**, 191–193.
- 34 ABAQUS Version 6.8-1**, User Documentation, Dassault Systems, 2008.
- 35 Ashby, M. F.** *Materials selection in mechanical design*, edition 3, 2005 (Elsevier Butterworth Heinemann, Oxford).
- 36 Johnson, G. R. and Cook, W. H.** A constitutive model and data for metals subjected to large strains, high strain rates and high temperatures. In *Proceedings of the 7th International Symposium on Ballistics*, 1983.
- 37 Kannan, K., Vetrano, J. S., and Hamilton, C. H.** Effects of alloy modification and thermomechanical processing on recrystallization of Al-Mg-Mn alloys. *Metallurg. Mater. Trans.*, 1996, **27A**, 22–33.
- 38 Reed-Hill, R. E.** *Physical metallurgy principles*, 1994 (PWS Publishing Company, Boston, Massachusetts).
- 39 Kocks, U. F., Argon, A. S., and Ashby, M. F.** Thermodynamics and kinetics of slip. *Prog. Mater. Sci.*, 1975, **19**, 1.

Q6

TO: CORRESPONDING AUTHOR

AUTHOR QUERIES - TO BE ANSWERED BY THE AUTHOR

The following queries have arisen during the typesetting of your manuscript. Please answer these queries by marking the required corrections at the appropriate point in the text.

Query number	Query Details
Q1	No keywords included. Are these OK?
Q2	Refs 9-12 are not cited. Please put in (note order may have to change if they are not in sequence and see AQ3)
Q3	Refs 24-28 not cited. Please put in. However note that 27 and 28 are mentioned later with Fig. 9 and 26 is in Sec 3.3., 3.3.1, 3.3.2 and 3.3.3. It will really throw the order out if they are not mentioned earlier together.
Q4	Colour is mentioned in list for Fig. 7 (a) and (b) but paper has no colour. Text will have to be changed.
Q5	last para before Sec. 4. Cocks et al. here but ref is Kocks. Which spelling is correct?
Q6	Ref 36 needs place of Symposium
Q7	Colour is mentioned in captions for Figs 8, 9, and 10. Either the text will have to be changed or these should be in colour